

Damping reveals hidden dimensions in elastic metastructures through induced transparency

Yanghao Fang^{1,‡}, William Tuxbury^{2,†}, Abhishek Gupta^{1,§}, Tsampikos Kottos^{1,2,*}, and Ramathasan Thevamaran^{1,3,†}

¹Department of Materials Science and Engineering, University of Wisconsin-Madison, Madison, Wisconsin 53706, USA

²Wave Transport in Complex Systems Lab, Department of Physics, Wesleyan University, Middletown, Connecticut 06459, USA

³Department of Mechanical Engineering, University of Wisconsin-Madison, Madison, Wisconsin 53706, USA

(Received 29 January 2024; revised 3 April 2024; accepted 15 April 2024; published 9 May 2024)

Damping typically results in attenuation of vibrations and elastic wave propagation in mechanical systems. Contrary to this conventional understanding, we demonstrate experimentally and explain theoretically the revival of an elastic wave transmitted through a periodic metastructure when a weak non-Hermitian defect (damping mechanism) induces violation of time-reversal symmetry. Damping alters the nature of the system's resonant modes, instigating interference in the scattering field. This leads to transmission revival, revealing the presence of hidden modes, which are otherwise masked by the symmetry. Our findings offer an approach for designing dissipation-driven switches and controllers and nondestructive structural health-monitoring systems.

DOI: 10.1103/PhysRevApplied.21.054022

I. INTRODUCTION

Defects in the geometry or mass of a periodic system have commonly been used to elicit distinct elastic or acoustic wave phenomena not present in perfectly periodic configurations [1], such as one-way wave propagation [2], bifurcation-based mechanical rectification [3], mechanical energy localization [4], nonlinear acoustic diodes [5], bounded modes [6,7], and topologically protected states [8,9]. While these theories predominantly focus on conservative (Hermitian) defects, which violate translational invariance, the introduction of localized energy amplification and/or attenuation-defect mechanisms (non-Hermitian) [10,11] also violates time-reversal symmetry, leading to unexpected phenomena, such as anomalous actuation-force (emissivity) enhancement [12], hypersensitive sensing [13–18], shadow-free sensing [19], and unidirectional invisibility [20,21]. For recent reviews on the implementation of symmetries (and their violation) in non-Hermitian structures in a variety of frameworks, including pressure acoustics, see Refs. [22,23].

Here, we demonstrate experimentally and explain theoretically that integrating a weak non-Hermitian defect—characterized by energy dissipation or damping—into an otherwise Hermitian metastructure can

lead to a counterintuitive phenomenon: the revival of longitudinal wave transmission when the system is excited from its plane-of-parity symmetry, as illustrated in Fig. 1(a). This observation challenges the conventional understanding that damping is an attenuation mechanism and extends the utility of damping beyond its common use in wave attenuation or vibration mitigation. In fact, similar unexpected phenomena have been observed in the photonics framework where gain reduction (by added loss) leads to lasing action [10,24,25].

In our mechanical paradigm, impulse excitation experiments [Fig. 1(b)] guided by finite-element (FE) analysis and coupled-mode-theory (CMT) modeling reveal a loss-induced resurgence of transmission at frequencies corresponding to antisymmetric eigenmodes of the metastructure. While the spatial parity-symmetry violation is observable from the destruction of the nodal point, our theoretical model points to a profound insight: the irreversibility introduced by damping violates the time-reversal symmetry of the metastructure, introducing a phase lag to the motion of the individual components of the metastructure. The alteration of the eigenmode nature (from real to complex-valued components), reinstates the contribution of a hidden mode in the transmission, leading to its revival, which is anomalously enhanced in the weak-damping regime. Specifically, the CMT analysis predicts a linear growth of transmittance for weak damping strengths compared to, for example, the enhancement due to purely geometric (nondissipative) defects, which demonstrate a

*Corresponding author: tkottos@wesleyan.edu

†Corresponding author: thevamaran@wisc.edu

‡Y. Fang and W. Tuxbury contributed equally to this work.

(weaker) quadratic growth of transmittance in the limit of small perturbations.

II. RESULTS AND DISCUSSION

A. Finite-element modeling

We use steady-state dynamic analyses in the commercial FE software SIMULIA Abaqus to model a periodic metasstructure featuring a non-Hermitian defect. This metasstructure comprises $2N + 1$ cross beams, with N cross beams on each side and one in the center. In FE modeling, we use an N_5 (i.e., $N = 5$) periodic metasstructure, which has five elastic cross beams on each side, and the first cross beam on the right side, counting outwards from the center (i.e., the 7th cross beam counting from the left side), has a

damping mechanism that introduces non-Hermiticity into the system. Each cross-beam section, extending from the tip to its junction with the horizontal beam, is 110 mm in length, with adjacent sections separated by a 20-mm center-to-center gap. The horizontal beam has 20-mm ledges on both ends. The whole metasstructure is defined as aluminum (with a Young's modulus of 68.9 GPa, a density of 2700 kg m^{-3} , and a Poisson's ratio of 0.33) and contains a uniform rectangular cross section [5 mm wide and 10 mm thick, as shown in the yellow inset in Fig. 1(b)]. We use three-node quadratic Timoshenko beam elements for the mesh, and both the cross-beam sections and the interval segment of the horizontal beam comprises 20 elements. The loss mechanism is modeled by the structural damping rate, γ .

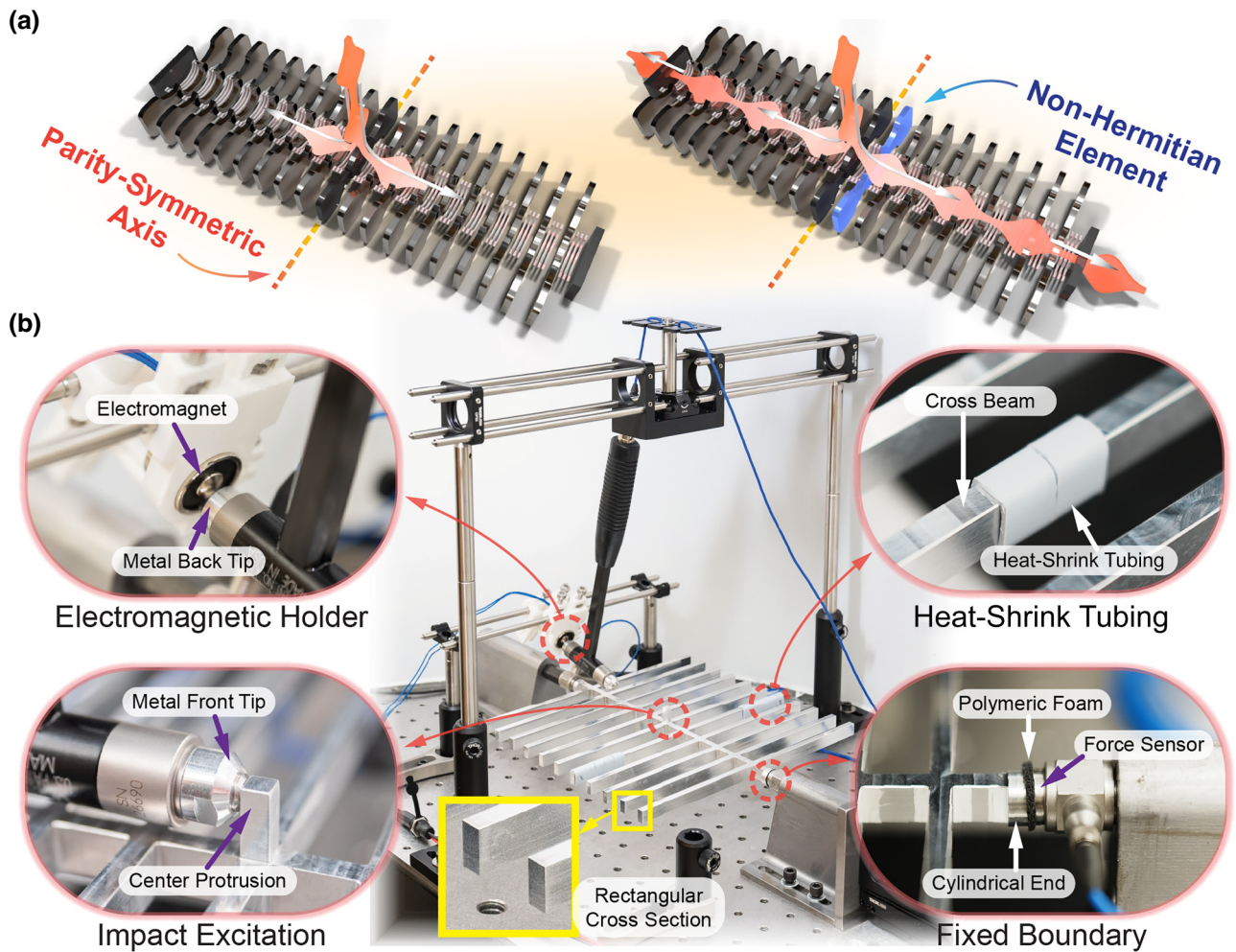


FIG. 1. Illustrations and experimental setup pictures of transmission revival in a periodic metasstructure with a non-Hermitian defect. (a) Transmission-signal variation before (left) and after (right) introducing a non-Hermitian defect when the system is excited from its center. (b) Custom-built impulse experiment apparatus showing an electromagnetic holding (releasing) mechanism for the repeatable impulse excitation by a hammer (top-left inset), impulse excitation by the instrumented hammer at the center of the metasstructure (bottom-left inset), heat-shrink tubing on the cross beam used for damping (top-right inset), and metasstructure boundaries supported by dynamic force sensors on either side with a polymeric foam placed between them to achieve uniform contact for transmission measurements (bottom-right inset). Bottom-middle inset shows the rectangular cross section of the beam.

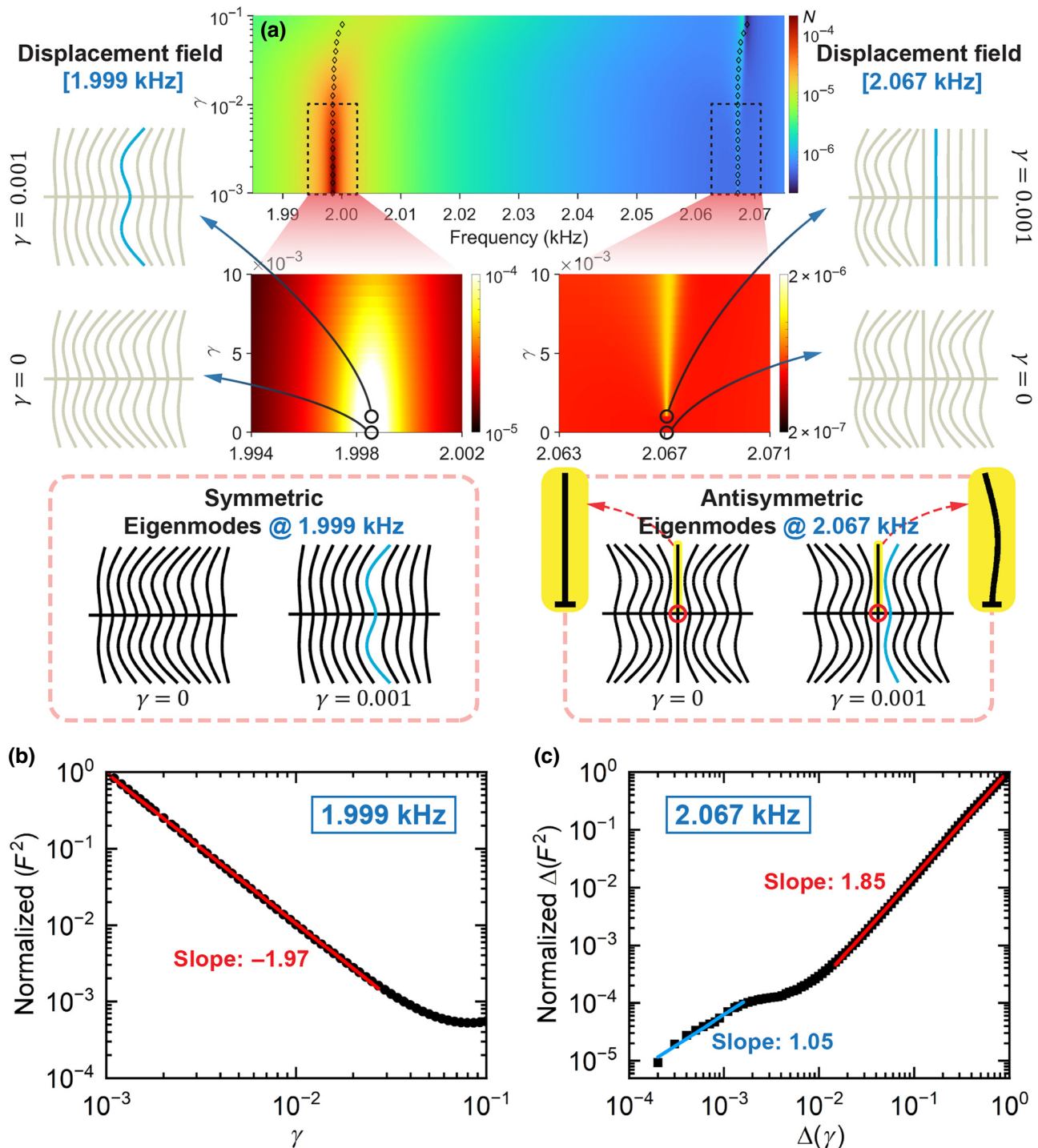


FIG. 2. Transmitted signals under center excitation of the metastructure. (a) Color-density plots (using FE analysis) of transmitted force overlaid by eigenvalue calculations (represented as black hollow diamonds) between 1.985 and 2.085 kHz as the damping intensity, γ , varies between 0.001 and 0.1. Insets on the left and right sides illustrate the displacement fields (non-Hermitian components are in blue) for two modes located at 1.999 and 2.067 kHz when $\gamma = 0$ (Hermitian) and $\gamma = 0.001$ (non-Hermitian), respectively. Corresponding eigenmodes are shown below enclosed in red dashed boxes. For the eigenmodes at 2.067 kHz, red circles indicate the locations of the center nodes, and yellow regions depict the slight deformation difference of the center beam as γ increases from 0 to 0.001. (b) Square of the normalized force intensity (normalized F^2 , which is proportional to the transmitted power) versus damping intensity, γ , for the mode at 1.999 kHz. Fitting slope of -1.97 represents the decay ratio. (c) Variation in the square of the normalized output force for the mode at 2.067 kHz [denoted as $\Delta(F^2) \equiv F^2 - F_{\gamma=0.001}^2$] plotted against the increase in damping [$\Delta(\gamma) \equiv \gamma - 0.0009$]. Slopes within the weak-damping and strong-damping regions are 1.05 ± 0.05 and 1.854 ± 0.005 , respectively.

To study how the strength of non-Hermiticity (damping strength γ) affects transport, we calculate the reaction-force signal under center excitation (parity-symmetry plane of the metastructure) as we increase the damping intensity. To further understand the effects of the excitation conditions, we have also performed a study under edge excitation, the results of which can be found in Fig. 4 in Appendix A. The center excitation is operated when the metastructure is excited harmonically with a prescribed longitudinal force of $1 \mu\text{N}$ at the metastructure's center while the ends are kept fixed and the transmission signal is collected from the fixed end located on the side without the damping component; the edge excitation is operated when one edge of the metastructure is excited harmonically with a prescribed longitudinal displacement of $1 \mu\text{m}$ while the other end remains fixed (i.e., zero displacement and rotation) and the transmission signal is collected from the fixed end.

Color-density plots of the transmission response corresponding to the center excitation can be seen in Fig. 2(a), together with the displacement fields and selective eigenmodes. The reaction-force magnitude was calculated from the fixed left end, where there is no damping element, and the eigenmodes of the metastructure are calculated under the boundary conditions where both ends are fixed. The two eigenvalues that exist between 1.985 and 2.085 kHz are represented by the black diamonds shown atop the density plot and their trajectories overlap with the resonance-peak locations found in the FE model. The insets on either side show the displacement fields of the two modes in the spectrum for two values of $\gamma = 0$ and $\gamma = 0.001$. The left column shows the displacement fields of a (typical) mode at 1.999 kHz, which demonstrates the same features with its corresponding eigenmodes. For $\gamma = 0$, the eigenmode is symmetric, since its corresponding elements on both parity-symmetric (P -symmetric) halves of the metastructure move in the same direction simultaneously, thus respecting the symmetry of the metastructure (as expected). This similarity between the displacement field and the eigenmode also persists for $\gamma = 0.001$. In contrast, the displacement fields corresponding to the mode at 2.067 kHz are different from the associated eigenmode for both $\gamma = 0$ and $\gamma = 0.001$, as evident in the right insets of Fig. 2(a). Specifically, for $\gamma = 0$, the eigenmode is antisymmetric (respecting the parity symmetry of the metastructure) with its two P -symmetric halves moving in opposite directions, resulting in a nodal point at the center (highlighted with a red circle). Its displacement field, however, is symmetric due to the center excitation disrupting the nodal point. When a small amount of damping is introduced ($\gamma = 0.001$) the eigenmode maintains its overall parity behavior [strictly speaking, a small imaginary part of the components is acquired, and the center beam starts to deform slightly, as shown in the yellow regions near the antisymmetric

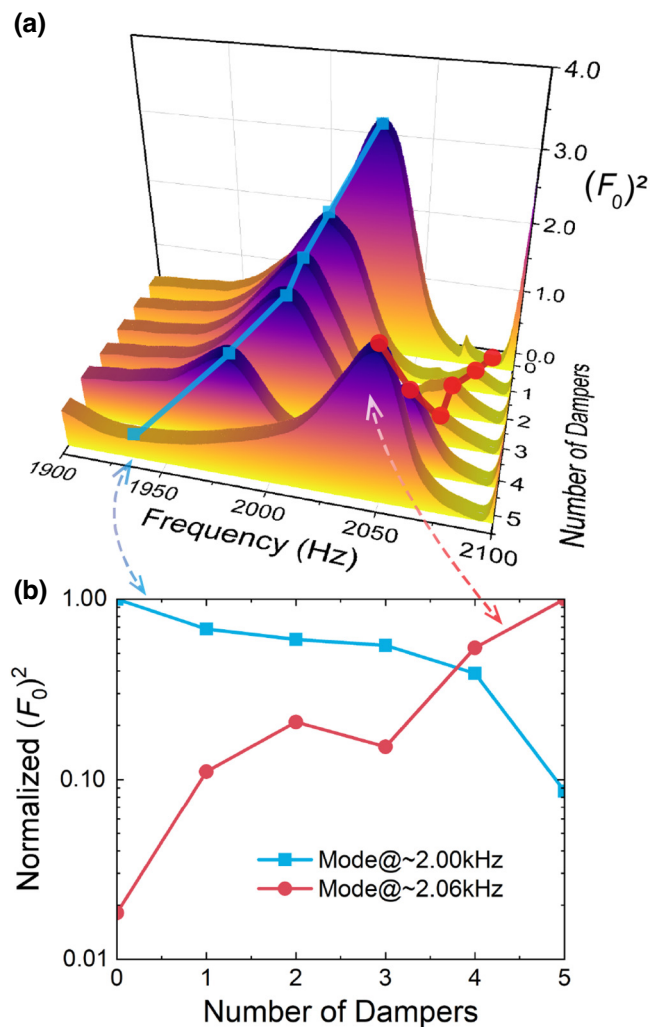


FIG. 3. Transmission revival in experiments. (a) Square of the transmission response between 1.9 and 2.1 kHz of the metastructure versus number of dampers. Amplitude $(F_0)^2 = (|F_s| \times |F_h|^{-1})^2$ is proportional to the transmitted power, with F_s and F_h denoting signal amplitudes from the force sensor and hammer in their Fourier representations, respectively. (b) Variation of the amplitudes $(F_0)^2$ corresponding to the two distinct modes near 2.00 and 2.06 kHz (normalized by their corresponding local maxima) as functions of number of dampers.

eigenmodes in Fig. 2(a)], while the corresponding displacement field experiences an abrupt parity violation originating from a superposition of symmetric and antisymmetric eigenmodes.

For a better understanding of the variation of the transmitted power—which is proportional to the square of the transmitted force, F^2 —with respect to damping intensity, γ , Fig. 2(b) presents the mode at 1.999 kHz. The fitting slope of -1.97 implies that $F^2 \propto \gamma^{-1.97}$, indicating a conventional transmitted power decay due to damping. Figure 2(c) shows how the transmitted power of the mode at 2.067 kHz varies with increasing damping. For weak damping, the variation behaves like $\Delta(\gamma)^\alpha$, where

the value of $\alpha = 1.05 \pm 0.05$ is evaluated from a least-squares fitting after extracting the asymptotic ($\gamma \rightarrow 0$) value of the transmittance from the SIMULIA Abaqus simulations. For stronger damping, the least-squares fit of the SIMULIA Abaqus data of the square of the transmitted force indicates a power-law variation that behaves like $\Delta(\gamma)^\alpha$, where $\alpha = 1.854 \pm 0.005$. These results are in qualitative agreement with the CMT prediction of transmittance for the frequency associated with the antisymmetric mode. In fact, CMT predicts a linear variation for small γ values. As loss increases, the resonant detuning (real part) of the defect-mode frequency dominates the behavior of the transmittance. In the extreme limit, where the defect resonant variation is completely dominated by its real part, CMT predicts quadratic behavior of the transmittance with respect to variations of the defect magnitude, in agreement with the SIMULIA Abaqus simulations (see Sec. II C and Appendix B). It is worth noting that such behavior only occurs at the frequencies corresponding to antisymmetric modes, and the symmetric modes are attenuated similarly to the behavior of the mode at 1.999 kHz. In P -symmetric metastructures excited by longitudinal waves, eigenmodes alternate between symmetric and antisymmetric profiles. Consequently, this characteristic of transmission revival persists across different spectral bands, system sizes, and defect locations, excluding the nodal point corresponding to an antisymmetric mode (see Figs. 5 and 6 in Appendix A). If the defect is located at the nodal point corresponding to a particular antisymmetric mode, there will be no transmission revival at that mode's frequency. Any other defect location can lead to transmission revival.

B. Impulse experiments

The metastructure is fabricated from monolithic aluminum 6061-T6 using CNC machining under the basic geometry in the FE model. As shown in Fig. 1(b), our sample was placed between two dynamic force sensors (PCB 208C01). Considering the shape of the force sensors, we designed the tips of the main beam's ends with two flat cylinders, each 12.7 mm in diameter, while keeping the total length consistent. We applied a precompression to prevent loss of contact with the force sensors and sliding, and we introduced protrusions at the center of the main beam for center excitation of the metastructure with an instrumented impact hammer (PCB 086C01). To accurately control the hammer impulse with reproducibility, we devised a rotational mechanical hammer-suspension mechanism coupled with an electromagnetic hammer-hold (-release) system, as shown in the insets of Fig. 1(b). We introduced damping to both sections of the seventh cross beam of the metastructure, counting from the left side, by affixing shrunken heat-shrink tubing to the tips. Each tubing segment weighed 0.422 g ($\pm 1\%$), accounting

for roughly 2.8% of the aluminum cross-beam section's weight of 14.85 g.

We measured time-domain signals from both the instrumented hammer and the dynamic force sensors during impact. After denoising by reserving only the pulse signal from the hammer and removing signals prior to impact from the force sensor, we used fast Fourier transform to transform these signals into the frequency domain. The hammer impulse excited frequencies up to approximately 3 kHz. We subsequently normalized the force sensors' signal, where the normalized force was $F_0 = |F_s| \times |F_h|^{-1}$, with F_s and F_h denoting signal amplitudes from the force sensor and hammer in their Fourier representations, respectively.

Figure 3 shows that the transmitted power of the mode near 2.00 kHz diminishes and shifts slightly to a lower frequency as the damping is increased, indicating a typical energy attenuation. In contrast, the mode at 2.06 kHz appears spontaneously when damping is introduced, and its transmitted power increases rapidly as damping is increased further—signifying a transmission-revival phenomenon. Specifically, the amplitude of the transmitted power increases by 2 orders of magnitude from the “0 dampers” (i.e., no dampers) to “5 dampers” (i.e., damping introduced by 5 heat-shrink tubing dampers on both ends of the cross beam). It is noteworthy that introducing damping using heat-shrink tubing will inevitably add extra mass ($\sim 2.8\%$ per tubing) to the defect beam, which causes some shift in the mode frequency, but we show later in our CMT analysis that the effects due to such geometric defects is small compared to the introduced damping.

C. CMT model

To describe the theoretical underpinnings of the computational and experimental results presented in the previous sections, we have developed a simplified model based on CMT [26], which allows us to theoretically explain the observed strong transmission revival for weak dissipations. The fundamental modes associated with the cantilever-free vibration of the isolated cross beams can be modeled as a one-dimensional array of $2N + 1$ isolated resonances with frequency ω_0 and nearest-neighbor coupling κ . Meanwhile, non-Hermiticity introduced by damping on the $N + l + 1$ element can be incorporated by the imaginary term $-i\gamma$. Therefore, the Hamiltonian operator of the closed system is expressed in the form $\hat{H} = \sum_{n=1}^{2N+1} \omega_0 |n\rangle \langle n| + \sum_{n=1}^{2N} \kappa |n\rangle \langle n+1| + c.c. - i\gamma |N+l+1\rangle \langle N+l+1|$, where $|n\rangle$ indicates the isolated mode of the n th cross beam. The system can then be turned into a scattering setup by attaching transmission lines (TLs) to the respective isolated resonances, which are accounted for by incorporating an imaginary self-energy correction to those diagonal matrix elements, leading to the effective Hamiltonian, $\hat{H}_{\text{eff}} = \hat{H} - (i/2)\hat{D}\hat{D}^T$. Here,

$\hat{D} = \sqrt{2\gamma_e} (|1\rangle\langle e_1| + |N+1\rangle\langle e_2| + |2N+1\rangle\langle e_3|)$ is referred to as the coupling matrix, where $|e_m\rangle$ indicates the flux-normalized propagating modes in the m th TL and γ_e encodes the coupling coefficient to those isolated resonances.

Using the Green function approach, we are able to acquire analytical expressions for the transmittance to the leftmost TL, due to a center excitation at frequency $\omega = \omega_0$ with respect to the non-Hermitian defect perturbation, where tildes indicate the quantities are normalized by the nearest-neighbor coupling κ :

$$T(\tilde{\gamma}) = \left[\frac{2\tilde{\gamma}_e(\tilde{\gamma}_e + \tilde{\gamma})}{(\tilde{\gamma}_e + \tilde{\gamma})(\tilde{\gamma}_e^2 + 1) + \tilde{\gamma}_e} \right]^2. \quad (1)$$

Inspection of Eq. (1) leads to the immediate conclusion that *the variation in the transmittance is first order in the damping parameter*, $T(\tilde{\gamma}) \approx T(0) + (8\tilde{\gamma}_e/((2 + \tilde{\gamma}_e)^3))\tilde{\gamma}$. In the case of zero damping perturbation, there is a background transmittance, $T(0) \neq 0$, associated with the contribution of nearby (symmetric) resonances of the composite metastructure, referred to as supermodes, at which point the hidden mode is undetectable. In the derivation, we have assumed N and l are both odd, so the defect resides on an antinode of the unperturbed antisymmetric supermode. Otherwise, the expression is independent of the system size and the defect's position.

To highlight the importance of the (weak) dissipative defect in the observed (strong) transmittance revival, we contrast the above results with a Hermitian (geometric) nondissipative defect, $\Delta \in \mathbb{R}$. In this case, the transmittance takes the form, $T(\tilde{\Delta}) = ((4\tilde{\gamma}_e^2(\tilde{\gamma}_e^2 + \tilde{\Delta}^2))/((\tilde{\gamma}_e^2 + \tilde{\Delta}^2)(\tilde{\gamma}_e^2 + 1)^2 + 2\tilde{\gamma}_e^2(\tilde{\gamma}_e^2 + 1) + \tilde{\gamma}_e^2))$, also following the same tilde notational convention as in the non-Hermitian case. The variation in the transmittance in the case of a Hermitian defect turns out to be a second-order effect of the defect strength, $\tilde{\Delta}$, i.e., $T(\tilde{\Delta}) \approx T(0) + ((4(3 + 2\tilde{\gamma}_e^2))/((2 + \tilde{\gamma}_e)^4))\tilde{\Delta}^2$, which for weak perturbations is much smaller than the previous results for dissipative defects. Such a comparative analysis indicates that time-reversal symmetry violation plays a significant role in uncovering the hidden mode via its contribution to the transmittance.

In Appendix B, we analyze the effect that nodal points of antisymmetric eigenmodes have on the transmittance in detail and relate the phenomena to a single-sided resonance [27,28]. Additionally, we use first-order nondegenerate perturbation theory to study the impact of a non-Hermitian defect on the eigenfrequency and nodal points of the unperturbed antisymmetric eigenmode. The calculation demonstrates that, in addition to the P -symmetry violation, which fundamentally disrupts the nodal point, broken time-reversal symmetry introduces a phase change into the components of the eigenmodes, resulting in interference between the supermodes comprising the scattering field

and leading to an enhanced (over Hermitian perturbations) transmittance revival. An important benefit of these dissipative perturbations is the fact that they do not distort the resonant frequency, while only increasing the resonance linewidth. The theoretical predictions provided by the CMT model underscore the utility of violating hidden (time-reversal) symmetries in the design and application of mechanical wave devices based on symmetry-management techniques.

III. CONCLUSIONS

We experimentally, computationally, and theoretically studied the transmission properties of an elastodynamic metastructure with an embedded non-Hermitian (damping) defect. We observed an emergence of the transmittance at frequencies associated with antisymmetric eigenmodes of the underlying Hermitian metastructure upon tuning the damping strength of the defect, revealing those hidden dimensions of the system. This phenomenon is independent of the system's size, the spectral band, and the location of defects as long as the defect does not lie at a nodal point. Our CMT model demonstrates that integration of a non-Hermitian defect enables otherwise obstructed energy transport by disrupting the central nodal point of antisymmetric eigenmodes without shifting their frequency. Comparison to a purely geometric defect shows that violation of the hidden time-reversal symmetry by the damping element dramatically intensifies the resurgence for weak perturbations—a linear enhancement, in contrast to quadratic enhancement achievable with geometric defects. These findings show an intriguing counterintuitive approach for inducing mechanical-wave transparency by introducing energy-loss mechanisms into an otherwise Hermitian system. Our results underscore the potential of non-Hermitian physics in reshaping our understanding and ability to manipulate wave propagation in elastodynamic systems. Our proof-of-principle experiments have technological ramifications for applications in nondestructive structural health monitoring, and realization of dissipation-driven switches and controllers, especially when dissipative nonlinearities self-induce symmetry violations.

ACKNOWLEDGMENTS

Y.F., A.G., and R.T. acknowledge financial support from the UW-Madison MRSEC program (Grant No. 1720415), the DCSD program of the National Science Foundation (Grant No. NSF-CMMI-1925530), and the Army Research Office (Grant No. W911NF2010160). W.T. and T.K. acknowledge financial support from the DCSD program of the National Science Foundation (Grant No. NSF-CMMI-1925543) and the Simons Foundation for Collaboration in MPS No. 733698. We thank Professor Melih Eriten for the instrumented impact hammer.

APPENDIX A: FINITE-ELEMENT ANALYSIS

This appendix provides results from the FE analysis. Figure 4 presents the transmitted signal from edge excitation of the same metastructure featured in the manuscript. The displacement fields at 1.999 kHz and 2.067 kHz correspond closely to the eigenmodes displayed in Fig. 2(a).

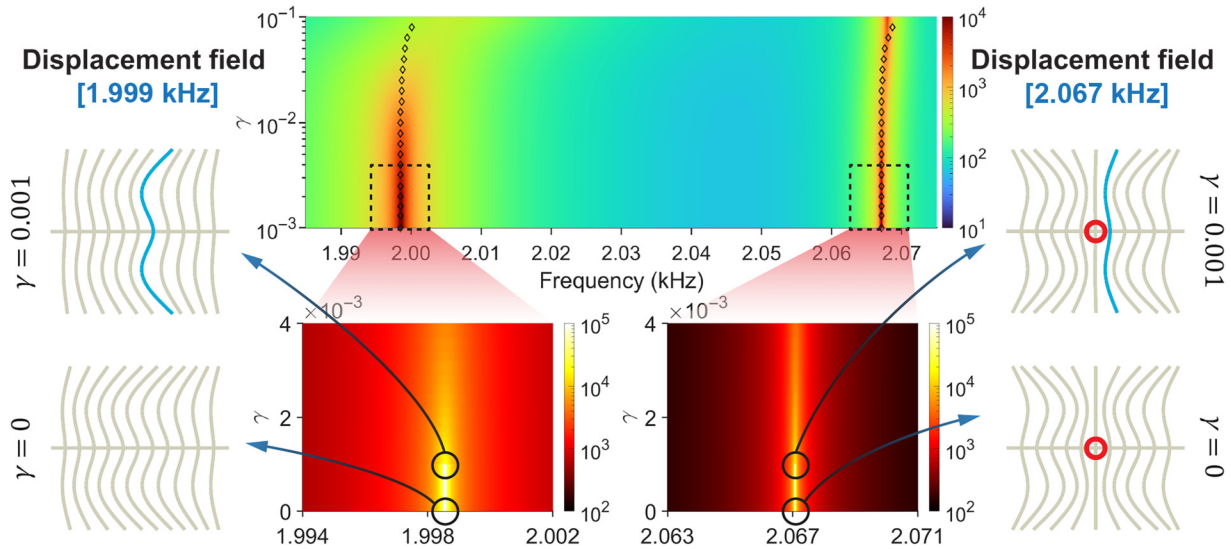


FIG. 4. Transmitted signal under edge excitation of the metastructure. Color-density plots (using FE analysis, unit is newton) overlaid by eigenvalue calculations (represented as black hollow diamonds) between 1.985 and 2.085 kHz as the damping intensity, γ , varies between 0.001 and 0.1. Insets on the left and right sides illustrate the displacement fields (non-Hermitian components are in blue) for modes at 1.999 and 2.067 kHz at $\gamma = 0$ (Hermitian) and $\gamma = 0.001$ (non-Hermitian), respectively. They are consistent with their eigenmodes due to their identical geometrical configurations.

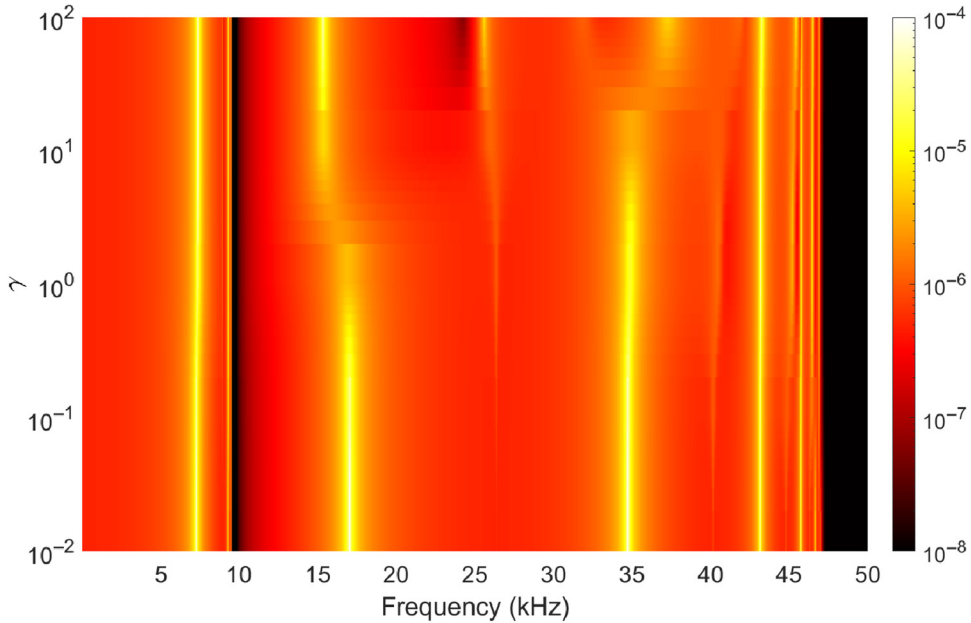


FIG. 5. Density plot of the transmitted signal for an N_5 metastructure (slightly different from the one used in the manuscript) under center excitation with a non-Hermitian defect (where damping intensity, γ , is added) on its first cross beam counting from the center. It displays a frequency range of 0 to 50 kHz and showcases two bands. First band is below 10 kHz, while the second spans approximately from 11 to 47 kHz. Notably, transmission revival is distinctly observable around 25 and 40 kHz, indicating its independence from the spectral bands. Please note that, due to resolution limitations, some instances of transmission revival might be challenging to observe without significant magnification.

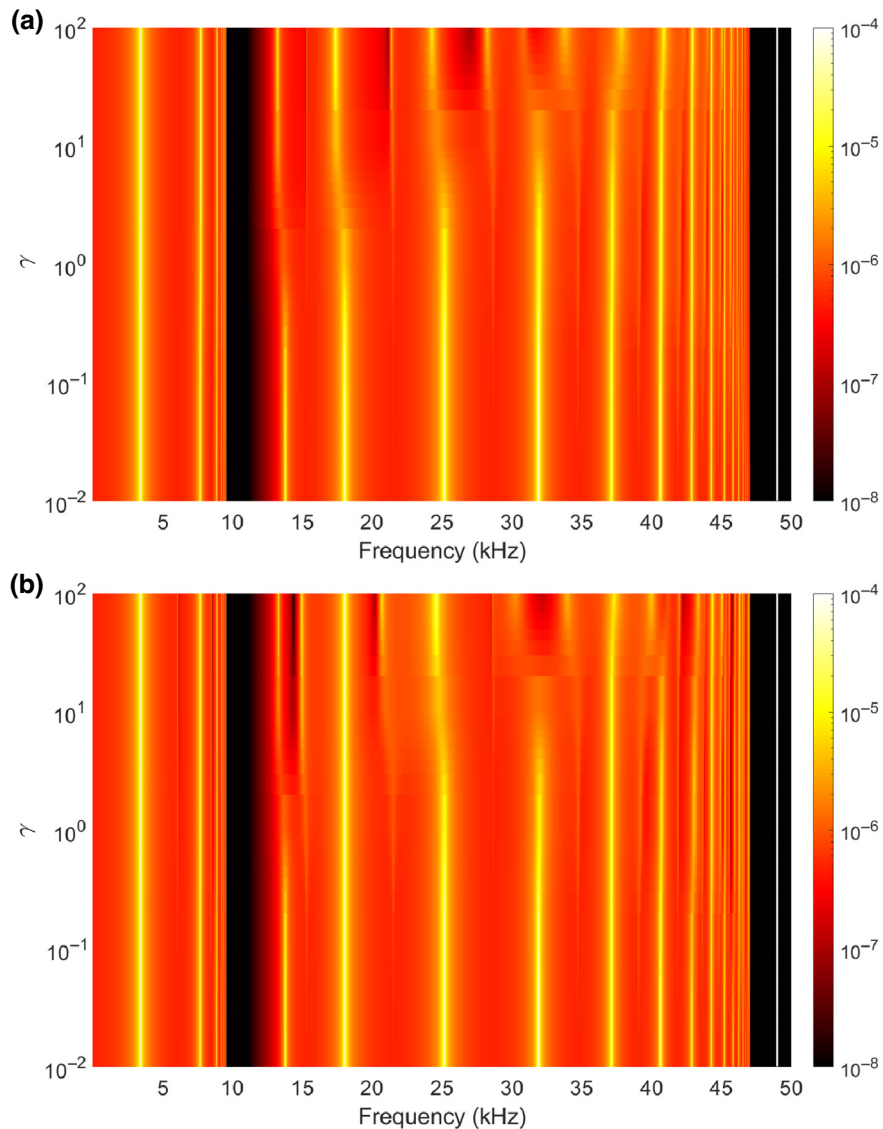


FIG. 6. Density plots of the transmitted signal for an N_{15} metastructure (belongs to the same group of metastructures as shown in Fig. 5) under center excitation when a non-Hermitian defect (where damping intensity, γ , is added) is embedded in different locations. (a) Defect is introduced on its first cross beam counting from the center. (b) Defect is introduced on its fifth cross beam counting from the center. Frequency range spans from 0 to 50 kHz and shows two bands, similar to Fig. 5. Similarly, transmission revival is observable at multiple frequencies, such as 22, 28, 35 kHz, etc., emphasizing its independence from system size and defect location. Please note that, due to resolution limitations, some instances of transmission revival might be challenging to observe without significant magnification.

Figures 5 and 6 show the transmitted signal from center excitation of a slightly different metastructure. These results demonstrate that the phenomenon of transmission revival can be observed across different spectral bands, system sizes, and defect locations.

APPENDIX B: COUPLED-MODE-THEORY ANALYSIS

1. Introduction

The purpose of this appendix is to detail the CMT analysis to provide a theoretical foundation for the computational and experimental results presented in the main text. The analysis summarized below only includes results obtained using the CMT formulation.

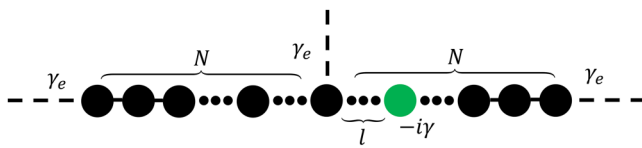


FIG. 7. Tight-binding schematic. System model is described in Eq. (B1) by a chain of $2N + 1$ resonators with uniform coupling, κ , and on-site potentials, ω_0 , along with loss, γ , introduced at the $N + 1 + l$ site. Isolated system is turned into a scattering setup by coupling leads to the center or ends of the array with coupling γ_e .

2. Model definition and effective Hamiltonian

The elastodynamics model associated with this research consists of a one-dimensional array of $2N + 1$ individual cross beams arranged transversely on a main connecting beam with a tunable loss element on the $N + l + 1$ cross beam. Considering the fundamental modes associated with the cantilever-free vibration associated with the isolated cross beams, the structure can be modeled using CMT as isolated resonances with frequency ω_0 and nearest-neighbor coupling κ via the main connecting beam. Meanwhile, non-Hermiticity introduced by loss on the $N + l + 1$ element can be incorporated by the imaginary term $-i\gamma$. Therefore, the Hamiltonian operator of the composite closed system is expressed on the basis of the isolated resonances as

$$\hat{H} = \sum_{n=1}^{2N+1} \omega_0 |n\rangle\langle n| + \sum_{n=1}^{2N} \kappa |n\rangle\langle n+1| + \text{c.c.} - i\gamma |N+l+1\rangle\langle N+l+1|. \quad (\text{B1})$$

Here, $|n\rangle$ represents the isolated mode of the n th cross beam, referred to hereafter as a site. The system can be turned into a scattering setup by attaching leads to the respective sites. Figure 7 shows a tight-binding schematic of the system. The perturbation of the leads can be modeled by an imaginary self-energy correction, which results in the effective Hamiltonian:

$$\hat{H}_{\text{eff}} = \hat{H} - \frac{i\hat{D}\hat{D}^T}{2}. \quad (\text{B2})$$

Here, $\hat{D} = \sqrt{2\gamma_e} (|1\rangle\langle e_1| + |N+1\rangle\langle e_2| + |2N+1\rangle\langle e_3|)$ is referred to as the coupling matrix, where $|e_m\rangle$ indicates the propagating modes of the m th lead and γ_e is the coupling coefficient to the coupled sites inside the structure. Physically, this corresponds to three symmetrically coupled scattering channels at the center and either side of the system. Therefore, the coupled-mode-theory equations are expressed as [26]

$$\omega|\psi\rangle = \hat{H}_{\text{eff}}|\psi\rangle + i\hat{D}|s^+\rangle, \quad (\text{B3a})$$

$$|s^-\rangle = \hat{D}^T|\psi\rangle - |s^+\rangle. \quad (\text{B3b})$$

Here, ω is the frequency of the interrogating monochromatic signal with incident wave front $|s^+\rangle = \sum_{m=1}^3 s_m^+ |e_m\rangle$, $|\psi\rangle = \sum_{n=1}^{2N+1} a_n |n\rangle$ denotes the steady-state scattering field inside the structure and $|s^-\rangle = \sum_{m=1}^3 s_m^- |e_m\rangle$ represents the outgoing wave front. The first of these equations describes internal dynamics with respect to an inhomogeneous driving term and the second encodes continuity of the input (output) waves and scattering field at the interface of the leads. Equation (B3a) can be rearranged to find the scattering field resulting from excitation due to the incident wave front:

$$|\psi\rangle = i\hat{G}\hat{D}|s^+\rangle, \quad (\text{B4})$$

where $\hat{G} = (\omega \mathbb{I}_{2N+1} - \hat{H}_{\text{eff}})^{-1}$ is the Green function and \mathbb{I}_M is the $M \times M$ identity matrix. Inserting Eq. (B4) into Eq. (B3b) results in the following input-output relationship:

$$|s^-\rangle = \hat{S}|s^+\rangle, \quad (\text{B5})$$

where $\hat{S} = -\mathbb{I}_3 + i\hat{D}^T\hat{G}\hat{D}$ is the scattering matrix.

3. Identification of symmetry-induced single-sided resonance

Omitting the explicit calculation, because it is geometrically apparent, the effective Hamiltonian is symmetric with respect to parity inversion in the absence of additional losses ($\gamma = 0$). The parity operator can be expressed on the basis of the sites:

$$\hat{P} = \sum_{n=1}^{2N+1} |n\rangle\langle 2N+2-n|. \quad (\text{B6})$$

It is well known [29] that parity-symmetric operators have eigenvectors that are either symmetric or antisymmetric. That is, symmetric and antisymmetric eigenmodes of the effective Hamiltonian, in the absence of additional losses, $\hat{H}_{\text{eff}}(\gamma = 0)|\psi_n\rangle = \omega_n |\psi_n\rangle$, represented on the basis of the sites as $|\psi_n\rangle = \sum_{n=1}^{2N+1} c_n |n\rangle$, satisfy $\hat{P}|\psi_n\rangle = \pm |\psi_n\rangle$, respectively. Consequently, antisymmetric modes (indicated by $n = n'$) have a nodal point on their center site:

$$\begin{aligned} \langle N+1|\psi_{n'}\rangle &= -\langle N+1|\hat{P}|\psi_{n'}\rangle \\ &= -\sum_{n=1}^{2N+1} \langle N+1|n\rangle\langle 2N+2-n|\psi_{n'}\rangle \\ &= \langle -N+1|\psi_{n'}\rangle \rightarrow c_{N+1} \\ &= \langle N+1|\psi_{n'}\rangle = 0. \end{aligned} \quad (\text{B7})$$

The presence of the nodal point in the wave functions enforces a single-sided resonance [27,28] because waves

incident from the center lead, at the corresponding energy, are blocked from entering the system. To understand this, we perform an eigenfunction expansion of the Green function in Eq. (B4), assuming an incident wave in proximity to an antisymmetric mode's eigenfrequency, $\omega_{n'}$, at the center lead, $|s^+\rangle = |e_2\rangle$:

$$\begin{aligned} |\psi(\omega = \text{Re}(\omega_{n'}))\rangle &= i \sum_{n=1}^{2N+1} \frac{|\psi_n\rangle \langle \psi_n|}{\omega - \omega_n} \hat{D} |e_2\rangle \\ &\approx i\sqrt{2\gamma_e} \langle \psi_{n'} | N + 1 \rangle |\psi_{n'}\rangle = 0. \end{aligned} \quad (\text{B8})$$

The approximate equality assumes lead-coupling coefficients are sufficiently small compared with the level spacing, so that $\text{Im}(\omega_n) \approx 0$, and thus, the other terms can be truncated from the summation. Despite \hat{H}_{eff} being a non-Hermitian operator, Eq. (B8) uses the appropriately normalized left eigenvectors for $\langle \psi_n|$, so that a biorthogonal inner product can be preserved, $\langle \psi_n | \psi_m \rangle = \delta_{nm}$.

Using Eq. (B3), the validity of the approximation can be tested by computing the occupation values, $|a_n|^2$, of the resulting scattering field by projecting it onto the basis of the effective Hamiltonian, $a_n = i\sqrt{2\gamma_e} \langle \psi_n | N + 1 \rangle$. The results for excitation at frequencies $\omega = \text{Re}(\omega_n)$ for a symmetric and antisymmetric mode are displayed in Fig. 8. Notably, the occupation values are many orders smaller for the antisymmetric mode frequency, compared with the symmetric mode frequency. Not only this, but the resulting scattering field at the antisymmetric frequency consists entirely of symmetric eigenmode components.

4. First-order perturbation theory of non-Hermitian elements

The eigenvalue problem for the closed Hermitian system, $\gamma = 0$, defined by

$$\omega_n^0 |\psi_n^0\rangle = \hat{H} |\psi_n^0\rangle, \quad (\text{B9})$$

has the following analytical solution when $\omega_0 = 0$ and $\kappa = 1$ are set as the reference and scale [30]:

$$\begin{aligned} |\psi_n^0\rangle &= \frac{1}{\sqrt{2(N+1)}} \sum_{j=1}^{2N+1} \sin\left(\frac{\pi n}{2(N+1)} j\right) |j\rangle; \\ \omega_n^0 &= 2 \cos\left(\frac{\pi n}{2(N+1)}\right). \end{aligned} \quad (\text{B10})$$

Specifically, wave functions possessing nodal points in the center of their profile occur when n is even:

$$\begin{aligned} \langle N+1 | \psi_n^0 \rangle &= \frac{1}{\sqrt{2(N+1)}} \sum_{j=1}^{2N+1} \sin\left(\frac{\pi n}{2(N+1)} j\right) \\ &\quad \times \langle N+1 | j \rangle \\ &= \frac{1}{\sqrt{2(N+1)}} \sin\left(\frac{\pi n}{2}\right). \end{aligned} \quad (\text{B11})$$

To be more explicit, we focus on mode $n = N+1$, where N is assumed to be odd, unless otherwise specified, for which

$$\begin{aligned} |\psi_{N+1}^0\rangle &= \frac{1}{\sqrt{2(N+1)}} \sum_{j=1}^{2N+1} \sin\left(\frac{\pi}{2} j\right) |j\rangle; \\ \omega_{N+1}^0 &= 2 \cos\left(\frac{\pi}{2}\right) = 0. \end{aligned} \quad (\text{B12})$$

First-order nondegenerate perturbation theory prescribes the first-order correction to the wave function [31]:

$$|\psi_{N+1}^1\rangle = \sum_{\substack{n=1 \\ n \neq N+1}}^{2N+1} \frac{\langle \psi_n^0 | \hat{V} | \psi_{N+1}^0 \rangle}{\omega_{N+1}^0 - \omega_n^0} |\psi_n^0\rangle. \quad (\text{B13})$$

The perturbation matrix is $\hat{V} = -i\gamma |N+1+l\rangle \langle N+1+l|$ and the first-order correction can be calculated as

$$\begin{aligned} |\psi_{N+1}^1\rangle &= i\gamma \sum_{\substack{n=1 \\ n \neq N+1}}^{2N+1} \frac{\langle \psi_n^0 | N+1+l \rangle \langle N+1+l | \psi_{N+1}^0 \rangle}{\omega_n^0} |\psi_n^0\rangle \\ &= \frac{i\gamma}{(2(N+1))^{3/2}} \sum_{\substack{j,n=1 \\ n \neq N+1}}^{2N+1} \frac{\sin((\pi n/(2(N+1)))(N+1+l)) \sin((\pi/2)(N+1+l))}{\omega_n^0} \sin\left(\frac{\pi n}{2(N+1)} j\right) |j\rangle, \end{aligned} \quad (\text{B14})$$

which is nonzero when l is odd, where the unperturbed antisymmetric eigenfunction acquires its antinodes. Assuming this to be the case,

$$|\psi_{N+1}^1\rangle = \frac{i\gamma (-1)^{(N+l)/2}}{(2(N+1))^{3/2}} \sum_{\substack{j,n=1 \\ n \neq N+1}}^{2N+1} \frac{\sin((\pi n/2) + (\pi n l/(2(N+1)))) \sin\left(\frac{\pi n}{2(N+1)} j\right)}{\cos((\pi n/(2(N+1))))} |j\rangle. \quad (\text{B15})$$

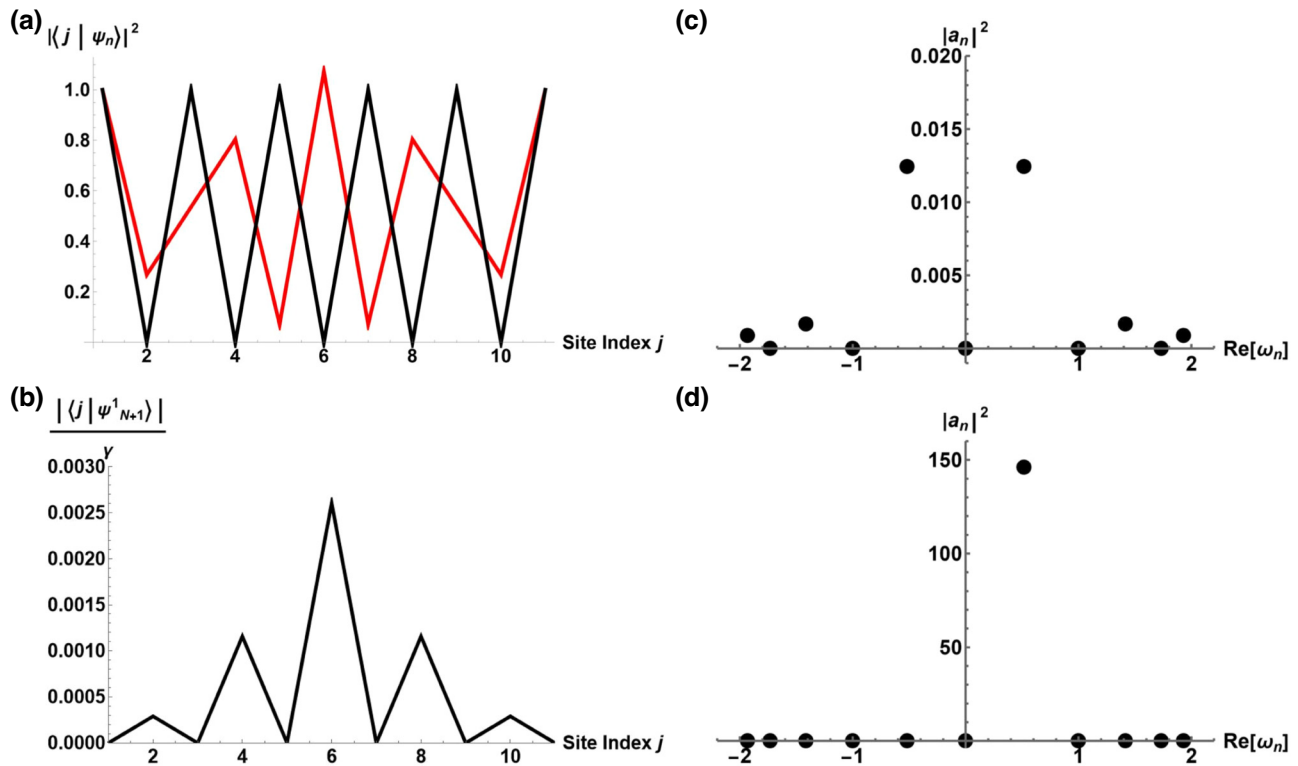


FIG. 8. Eigenmodes of parity-symmetric structure and projection of center excitation. (a) Intensity profile of eigenmodes corresponding to the closed Hermitian system with $N = 5$. Black line represents the $n = N + 1$ antisymmetric mode with a nodal point at site $j = N + 1$, and red line corresponds to the $n = N + 2$ symmetric mode, which has an antinode at its center. (b) Norm of first-order correction to antisymmetric eigenmode $n = N + 1$ due to non-Hermitian perturbation $-i\gamma$ to site $j = N + 1 + l$ for $l = 1$, demonstrating its function to destroy the nodal point. Occupation values of the scattering field resulting from center excitation with weak lead coupling, $\gamma_e = 10^{-2}$, driven at the real part of the eigenfrequency of modes (c) $n = N + 1$ and (d) $n = N + 2$. (e) Antisymmetric mode frequency indicates the scattering field is only composed symmetric modes due to their resonance overlap, while antisymmetric modes (in particular $n = N + 1$) are excluded from the superposition. (f) Projection at the symmetric mode frequency indicates that excitation is primarily comprised of the symmetric mode nearest to the driving frequency. Excited intensity is many orders smaller in the antisymmetric case due to the presence of a nodal point at the driven lead.

We see the partial effect of the non-Hermitian perturbation is to introduce a phase change into the eigenmodes of the system, which results in an interference between the modes of the scattering field. The norm of the correction is plotted in Fig. 9, where we see a strong disruption of the

nodal point. Of course, for weak coupling to the transmission lines, the above results also pertain to the shape of resonant modes.

Inspecting the effect of the perturbation on the nodal point, we find

$$\langle N+1 | \psi_{N+1}^1 \rangle = \frac{i\gamma}{2(2(N+1))^{3/2}} \sum_{\substack{n=1 \\ n \neq N+1}}^{2N+1} \frac{\sin((\pi n/2) + ((\pi n l)/(2(N+1))))}{\cos((\pi n/(2(N+1))))} \sin\left(\frac{\pi n}{2}\right). \quad (\text{B16})$$

Despite being unable to evaluate the summation in a closed form, a numerical investigation for various odd values of N , with respect to odd values of l , has indicated that nodal-point destruction is independent of defect placement and the size of the system, up to the normalization of the wave function due to the increasing number of sites.

Meanwhile, the first-order perturbation to the eigenvalues is provided by

$$\omega_n^1 = \langle \psi_n^0 | \hat{V} | \psi_n^0 \rangle, \quad (\text{B17})$$

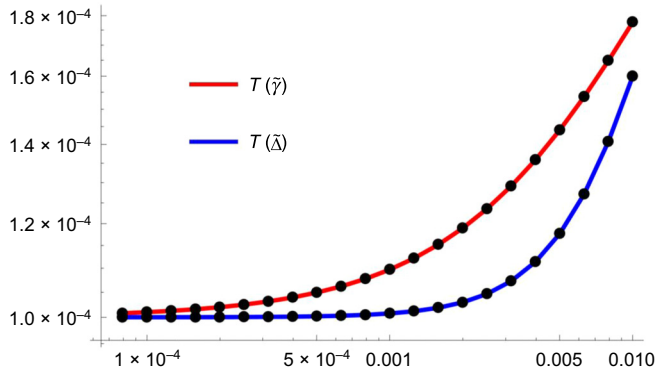


FIG. 9. Transmission resurgence for lossy and Hermitian defects. Vertical axis is transmission from the center lead to the leftmost lead, and horizontal axis indicates the perturbation strength of the defect. Red line is Eq. (B21b) plotted with respect to the strength of the non-Hermitian defect, $\tilde{\gamma}$. Blue line is Eq. (B22b) plotted with respect to the strength of the Hermitian defect, $\tilde{\Delta}$. Black points are numerical results simulated with weak coupling, $\tilde{\gamma}_e = 0.01$, for a system size of $2N + 1$ with $N = 5$, and defect placement, l , to the right of the center site, with $l = 1$ to verify the analytical expressions; however, the expressions are independent of odd values of N and l . Notably, transmission enhancement is linear with respect to $\tilde{\gamma}$ and quadratic with respect to $\tilde{\Delta}$. Therefore, non-Hermitian perturbation to the defect, counterintuitively, results in a more sudden increase in transmission than that of a Hermitian perturbation. This underscores the utility of simultaneously violating both geometric and hidden (time-reversal) symmetries in the design and application of mechanical wave devices.

which is evaluated as

$$\begin{aligned}\omega_n^1 &= -i\gamma |\langle N+1+l | \psi_n^0 \rangle|^2 \\ &= -\frac{i\gamma}{2(N+1)} \sin^2 \left(\frac{\pi n}{2} + \frac{\pi l}{2(N+1)} \right). \quad (\text{B18})\end{aligned}$$

Therefore, to first order, a non-Hermitian perturbation only has the effect of increasing the linewidth of the modes, without changing their resonant frequency. Meanwhile, a Hermitian perturbation would introduce a resonant shift to the mode frequencies, which is more inconvenient to track experimentally.

5. Analytical Green function and transmission revival

In this section, we calculate the transmission to the left-most lead from an incident signal at the center lead. Specifically, we are interested in the quantity $T = |\langle e_1 | s^- \rangle|^2$ due to the single-port excitation defined by $|s^+\rangle = |e_2\rangle$, driven at the eigenfrequency of an antisymmetric eigenmode of the unperturbed system (specifically, $\omega = \omega_0 = 0$, with N and l both odd). At this frequency, the Green function reduces to $\hat{G} = -(H_{\text{eff}})^{-1}$, corresponding to a tridiagonal matrix inversion. Since the coupling is assumed to be uniform, matrix elements of the inverse can be evaluated

analytically using [32]

$$-(H_{\text{eff}})_{ij}^{-1} = \begin{cases} (-1)^{i+j} \kappa^{|j-l|} \theta_{i-1} \phi_{j+1} / \theta_{2N+1}, & i < j, \\ \theta_{i-1} \phi_{j+1} / \theta_{2N+1}, & i = j, \\ (-1)^{i+j} \kappa^{|i-j|} \theta_{j-1} \phi_{i+1} / \theta_{2N+1}, & i > j. \end{cases} \quad (\text{B19})$$

Along with the following set of recursion relationships:

$$\theta_i = d_i \theta_{i-1} - \kappa^2 \theta_{i-2}; \quad i = 2, 3, \dots, 2N+1, \quad (\text{B20a})$$

$$\phi_i = d_i \phi_{i+1} - \kappa^2 \phi_{i+2}; \quad i = 2N, 2N-1, \dots, 1, \quad (\text{B20b})$$

where $d_i = -i [\gamma_e(\delta_{i,1} + \delta_{i,N+1} + \dots + \delta_{i,2N+1}) + \gamma\delta_{i,N+1+i}]$ are the diagonal elements of \hat{H}_{eff} , and the initial terms of the sequence are provided by $\theta_0 = 1$, $\theta_1 = -(H_{\text{eff}})_{11}$, $\phi_{2N+2} = 1$, and $\phi_{2N+1} = -(H_{\text{eff}})_{2N+1,2N+1}$. Once the Green function is obtained, an expression for the transmission coefficient can be obtained:

$$t = 2i\tilde{\gamma}_e \frac{\tilde{\gamma}_e + \tilde{\gamma}}{(\tilde{\gamma}_e + \tilde{\gamma})(\tilde{\gamma}_e^2 + 1) + \tilde{\gamma}_e}, \quad (\text{B21a})$$

where the tilde here indicates that the quantity is normalized by the coupling between sites of the system (i.e., $\tilde{\gamma} \equiv \gamma/\kappa$ and $\tilde{\gamma}_e \equiv \gamma_e/\kappa$). Correspondingly, the transmission can be computed using Eq. (B5). The result is

$$T = \left[\frac{2\tilde{\gamma}_e(\tilde{\gamma}_e + \tilde{\gamma})}{(\tilde{\gamma}_e + \tilde{\gamma})(\tilde{\gamma}_e^2 + 1) + \tilde{\gamma}_e} \right]^2. \quad (\text{B21b})$$

As a monotonically increasing function in $\tilde{\gamma}$, Eq. (B21b) demonstrates enhancement in the transmission as a response to the increasing strength of the non-Hermitian defect. Notably, this result is independent of the size of the system and defect placement, provided both N and l are odd. The reason the transmission does not vanish for $\gamma = 0$, despite \hat{H}_{eff} being parity symmetric, is due to overlapping resonances that are broadened by increasing the lead coupling, which is particularly significant for large values of $\tilde{\gamma}_e$. This fact regarding overlapping resonances can also be recognized from the occupation values presented in Fig. 8.

6. Impact of hidden symmetry violation

On the surface, the non-Hermitian perturbation only serves to violate the parity symmetry of the underlying structure. In fact, this is not the case. As discussed in the above perturbation-theory analysis, additional loss mixes the phases associated with unperturbed eigenmodes. Moreover, in the expression for the transmission coefficient, Eq. (B21a), the effect of a Hermitian defect can be studied by substituting the added loss with a resonant shift

of the isolated mode, Δ , i.e., $-i\tilde{\gamma} \rightarrow \tilde{\Delta}$. In this case, the transmission coefficient is

$$t = 2i\tilde{\gamma}_e \frac{\tilde{\gamma}_e + i\tilde{\Delta}}{(\tilde{\gamma}_e + i\tilde{\Delta})(\tilde{\gamma}_e^2 + 1) + \tilde{\gamma}_e}. \quad (\text{B22a})$$

So, from Eq. (B5), the transmission is computed as

$$T = \frac{4\tilde{\gamma}_e^2(\tilde{\gamma}_e^2 + \tilde{\Delta}^2)}{(\tilde{\gamma}_e^2 + \tilde{\Delta}^2)(\tilde{\gamma}_e^2 + 1)^2 + 2\tilde{\gamma}_e^2(\tilde{\gamma}_e^2 + 1) + \tilde{\gamma}_e^2}. \quad (\text{B22b})$$

The key feature to observe is, while Eq. (B21b) indicates an enhancement in the transmission that is first order in $\tilde{\gamma}$, the transmission enhancement from Eq. (B22b) is only second order in $\tilde{\Delta}$, due to the vanishing cross term. Therefore, in addition to violating parity symmetry, the non-Hermitian perturbation has the profound effect of also violating the hidden time-reversal symmetry, which results in a considerable impact on transmission revival, as demonstrated in Fig. 9. Furthermore, in the limit of extremely large defect strengths, both expressions approach the same value for transmittance. This is not surprising because, in either case, the second half of the system becomes decoupled entirely. Such a scenario is unrealistic in the experimental platform, where we consider small perturbations, i.e., $\tilde{\gamma}, \tilde{\Delta} \ll 1$.

- [1] H. Nassar, B. Yousefzadeh, R. Fleury, M. Ruzzene, A. Alù, C. Daraio, A. N. Norris, G. Huang, and M. R. Haberman, Nonreciprocity in acoustic and elastic materials, *Nat. Rev. Mater.* **5**, 667 (2020).
- [2] N. Swinteck, S. Matsuo, K. Runge, J. O. Vasseur, P. Lucas, and P. A. Deymier, Bulk elastic waves with unidirectional backscattering-immune topological states in a time-dependent superlattice, *J. Appl. Phys.* **118**, 063103 (2015).
- [3] N. Boechler, G. Theocharis, and C. Daraio, Bifurcation-based acoustic switching and rectification, *Nat. Mater.* **10**, 665 (2011).
- [4] S. Job, F. Santibanez, F. Tapia, and F. Melo, Wave localization in strongly nonlinear hertzian chains with mass defect, *Phys. Rev. E* **80**, 025602 (2009).
- [5] A. Darabi, L. Fang, A. Mojahed, M. D. Fronk, A. F. Vakakis, and M. J. Leamy, Broadband passive nonlinear acoustic diode, *Phys. Rev. B* **99**, 214305 (2019).
- [6] A. Rahman and R. K. Pal, Bound modes in the continuum based phononic waveguides, *J. Appl. Phys.* **132**, 115109 (2022).
- [7] A. Rahman and R. K. Pal, Elastic bound modes in the continuum in architected beams, *Phys. Rev. Appl.* **21**, 024002 (2024).
- [8] B. Xia, J. Zhang, L. Tong, S. Zheng, and X. Man, Topologically valley-polarized edge states in elastic phononic plates yielded by lattice defects, *Int. J. Solids Struct.* **239–240**, 111413 (2022).
- [9] Q. Wang, H. Xue, B. Zhang, and Y. D. Chong, Observation of protected photonic edge states induced by real-space topological lattice defects, *Phys. Rev. Lett.* **124**, 243602 (2020).
- [10] R. El-Ganainy, K. G. Makris, M. Khajavikhan, Z. H. Musslimani, S. Rotter, and D. N. Christodoulides, Non-Hermitian physics and PT symmetry, *Nat. Phys.* **14**, 11 (2018).
- [11] Y. Ashida, Z. Gong, and M. Ueda, Non-Hermitian physics, *Adv. Phys.* **69**, 249 (2020).
- [12] A. Gupta, A. Kurnosov, T. Kottos, and R. Thevamaran, Reconfigurable enhancement of actuation forces by engineered losses in non-Hermitian metamaterials, *Extreme Mech. Lett.* **59**, 101979 (2023).
- [13] R. Kononchuk, J. Cai, F. Ellis, R. Thevamaran, and T. Kottos, Exceptional-point-based accelerometers with enhanced signal-to-noise ratio, *Nature* **607**, 697 (2022).
- [14] M. I. N. Rosa, M. Mazzotti, and M. Ruzzene, Exceptional points and enhanced sensitivity in PT -symmetric continuous elastic media, *J. Mech. Phys. Solids* **149**, 104325 (2021).
- [15] V. Domínguez-Rocha, R. Thevamaran, F. M. Ellis, and T. Kottos, Environmentally induced exceptional points in elastodynamics, *Phys. Rev. Appl.* **13**, 014060 (2020).
- [16] A. Gupta and R. Thevamaran, Requisites on material viscoelasticity for exceptional points in passive dynamical systems, *J. Phys. Mater.* **6**, 035011 (2023).
- [17] Y. Fang, T. Kottos, and R. Thevamaran, Emergence of exceptional points in periodic metastructures with hidden parity-time symmetric defects, *J. Appl. Mech.* **89**, 121003 (2022).
- [18] Y. Fang, T. Kottos, and R. Thevamaran, Universal route for the emergence of exceptional points in PT -symmetric metamaterials with unfolding spectral symmetries, *New J. Phys.* **23**, 063079 (2021).
- [19] R. Fleury, D. Sounas, and A. Alù, An invisible acoustic sensor based on parity-time symmetry, *Nat. Commun.* **6**, 5905 (2015).
- [20] X. Zhu, H. Ramezani, C. Shi, J. Zhu, and X. Zhang, PT -Symmetric acoustics, *Phys. Rev. X* **4**, 031042 (2014).
- [21] Y. Aurégan and V. Pagneux, PT -Symmetric scattering in flow duct acoustics, *Phys. Rev. Lett.* **118**, 174301 (2017).
- [22] L. Huang, *et al.*, Acoustic resonances in non-Hermitian open systems, *Nat. Rev. Phys.* **6**, 11 (2023).
- [23] Z. Gu, H. Gao, P.-C. Cao, T. Liu, X.-F. Zhu, and J. Zhu, Controlling sound in non-Hermitian acoustic systems, *Phys. Rev. Appl.* **16**, 057001 (2021).
- [24] B. Peng, ŞK Özdemir, S. Rotter, H. Yilmaz, M. Liertzer, F. Monifi, C. M. Bender, F. Nori, and L. Yang, Loss-induced suppression and revival of lasing, *Science* **346**, 328 (2014).
- [25] L. Feng, R. El-Ganainy, and L. Ge, Non-Hermitian photonics based on parity-time symmetry, *Nat. Photonics* **11**, 752 (2017).
- [26] S. Fan, W. Suh, and J. D. Joannopoulos, Temporal coupled-mode theory for the Fano resonance in optical resonators, *J. Opt. Soc. Am. A* **20**, 569 (2003).
- [27] H. Zhou, B. Zhen, C. W. Hsu, O. D. Miller, S. G. Johnson, J. D. Joannopoulos, and M. Soljačić, Perfect single-sided radiation and absorption without mirrors, *Optica* **3**, 1079 (2016).

- [28] W. R. Sweeney, C. W. Hsu, and A. D. Stone, Theory of reflectionless scattering modes, *Phys. Rev. A* **102**, 063511 (2020).
- [29] J. J. Sakurai and J. Napolitano, in *Modern Quantum Mechanics* (Cambridge University Press, Cambridge, 2021), 3rd ed., pp. 256–264.
- [30] J. B. Marion and S. T. Thornton, in *Classical Dynamics of Particles & Systems*, edited by C. Hall, A. White, J. Lee, and J. M. DeSilva (Brooks/Cole, Belmont, 2004), 5th ed., pp. 498–505.
- [31] J. J. Sakurai and J. Napolitano, in *Modern Quantum Mechanics* (Cambridge University Press, Cambridge, 2021), 3rd ed., pp. 288–299.
- [32] C. M. da Fonseca, On the eigenvalues of some tridiagonal matrices, *J. Comput. Appl. Math.* **200**, 283 (2007).